

# Tailoring Permanent Charge Carrier Densities in Epitaxial Graphene on SiC by Functionalization with F4-TCNQ

Yefei Yin,\* Atasi Chatterjee, Davood Momeni, Mattias Kruskopf, Martin Götz, Stefan Wundrack, Frank Hohls, Klaus Pierz,\* and Hans W. Schumacher

The outstanding properties and the potential for large-scale fabrication open a wide field for electronic applications of epitaxial graphene on silicon carbide substrates. However, reliable doping methods to permanently control and tailor the carrier concentration to the desired value without applying an electrostatic gate are challenging and still under investigation. In this study, a post-growth molecular doping technique is investigated that compensates for the high electron density of pristine epitaxial graphene by using the acceptor F4-TCNQ. By precise adjustment of the dopant concentration, the carrier density can be tuned in a wide range from intrinsic *n*- to the *p*-type regime. The fabricated quantum Hall devices are ready-to-use, and no further treatments are required. High-precision resistance measurements of graphene-based devices with different doping levels show a quantization accuracy of  $10^{-9}$  that underlines the high quality of the fabricated devices and the suitability of this method for device applications. The experimentally observed correlation between the carrier density and the onset of the quantum Hall plateau gives a reliable criterion for the choice of devices in quantum resistance metrology.

## 1. Introduction

Epitaxial graphene is a promising candidate for the fabrication of future electronic devices. It combines outstanding material properties, like high electronic and thermal conductivity with the option for large-scale fabrication on silicon carbide (SiC) wafers and subsequent processing without transfer to another substrate.<sup>[1,2]</sup> The linear band structure (Dirac cone) near the *K*-point of this two-dimensional hexagonal carbon lattice enables a high mobility of electrons and holes, so-called massless relativistic Dirac fermions, and the observation of the quantum Hall effect (QHE) at room temperature.<sup>[3]</sup>

Y. Yin, A. Chatterjee, D. Momeni, M. Kruskopf, M. Götz, S. Wundrack, F. Hohls, K. Pierz, H. W. Schumacher  
Physikalisch-Technische Bundesanstalt  
Bundesallee 100, 38116 Braunschweig, Germany  
E-mail: yefei.yin@ptb.de; klaus.pierz@ptb.de

The ORCID identification number(s) for the author(s) of this article can be found under <https://doi.org/10.1002/apxr.202200015>

© 2022 The Authors. Advanced Physics Research published by Wiley-VCH GmbH. This is an open access article under the terms of the Creative Commons Attribution License, which permits use, distribution and reproduction in any medium, provided the original work is properly cited.

DOI: 10.1002/apxr.202200015

A prerequisite for developing graphene-based electronics is the reliable control of the charge carrier density that has been the key to the success of semiconductor technology in the past decades. Since as-grown epi-graphene already exhibits a high *n*-type carrier density of up to  $10^{13} \text{ cm}^{-2}$ ,<sup>[4]</sup> the goal is a controlled reduction, if possible, to the charge-neutrality point and beyond into the *p*-type regime. However, substitutional doping strongly increases charge carrier scattering that has a detrimental impact on the conductivity.<sup>[5]</sup> This goal has been achieved by electronic gating techniques with metal gates,<sup>[6]</sup> photo-chemical sensitive layers<sup>[7]</sup> or static surface charges.<sup>[8]</sup> Also molecular doping with acids, e.g. diluted aqua regia or nitric acid in combination with annealing procedures,<sup>[9–12]</sup> fluorinated fullerenes,<sup>[13]</sup> oxygen adsorption,<sup>[14,15]</sup> or metal atom adsorption (e.g. gold or antimony)<sup>[16]</sup> have been successfully applied to reduce the electron density and *p*-type conductivity of the epitaxial graphene layer could be achieved. A very successful route is the graphene functionalization with chromium tricarbonyl, which allows for stable, gateless, and reversible carrier density tuneability in quantum Hall resistance standards.<sup>[10,17]</sup> However, most of these techniques do not allow a permanent adjustment of the electronic properties or require adjustment in the users lab. Improved stabilities of doped graphene layers can be achieved, e.g. by applying passivation layers of PMMA,<sup>[14,15]</sup> dielectrics,<sup>[18]</sup> hexagonal boron nitride layers,<sup>[19,20]</sup> parylene,<sup>[21]</sup> or glass encapsulation.<sup>[22,23]</sup> First experiments with the molecular electron acceptor 2,3,5,6-Tetrafluor-7,7,8,8-tetracyanochinodimethan (F4-TCNQ), exhibited a considerable reduction of the electron density via a charge transfer mechanism.<sup>[1]</sup> Recent investigations of deposited F4-TCNQ doping stacks on epitaxial graphene revealed significant improvements in the long-term stability of the charge carrier density but precise tuning of the carrier density by post-annealing over a wide range remains challenging.<sup>[28,29]</sup> However, this is of importance for instance in quantum Hall resistance metrology where carrier densities in an optimal window are preferred. Values in the lower  $10^{11} \text{ cm}^{-2}$  range are necessary to be well above the charge puddle regime in which inhomogeneities destroy the QHE but low enough for enabling quantization at small magnetic fields.<sup>[30,31]</sup>

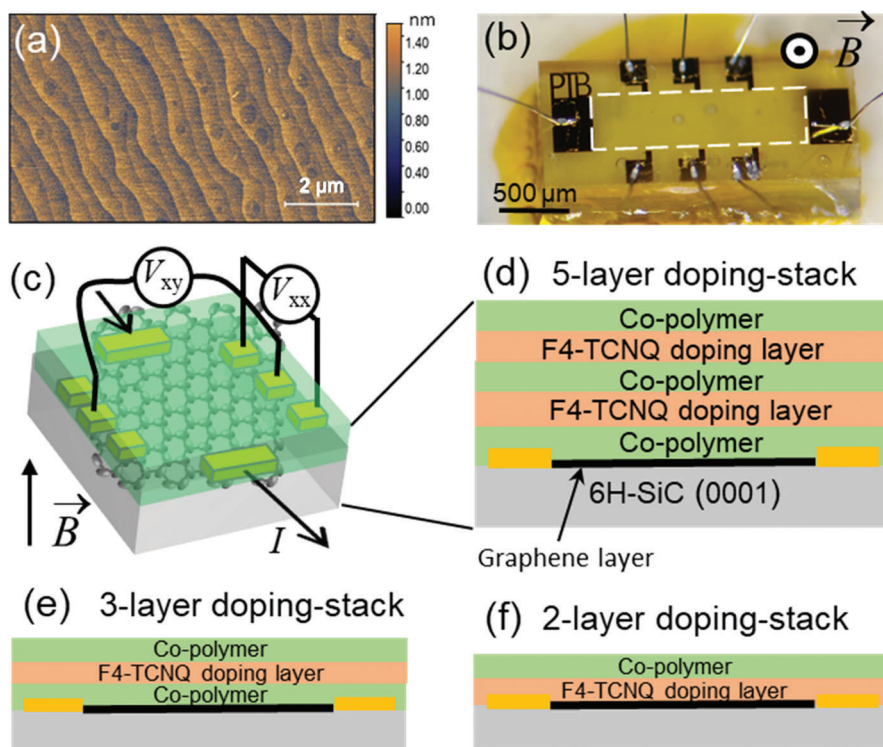


**Figure 1.** a) AFM image of a PASG grown graphene surface revealing ultra-low step heights and pure monolayer graphene. b) Photograph of a graphene-based Hall bar device. The dashed line indicates the graphene area. Graphene and the SiC substrate are transparent. c) Sketch of the Hall bar device and the wiring for longitudinal and Hall voltage measurements,  $V_{xx}$  and  $V_{xy}$ , respectively. d–f) Layer sequence of the 5-, 3- and 2-layer F4-TCNQ doping stack on top of the graphene layer. The thickness of each individual layers is  $\approx 100$  nm.

Here, we show that the carrier density of epitaxial graphene can be adjusted over a wide range in the  $n$ -type to the  $p$ -type regime by controlling the F4-TCNQ concentration in the overlying doping layer. Since we are dealing with a compensation doping process, it is essential to control and reliably reproduce the properties of the starting graphene layer as well as the initial carrier density. This was accomplished by fabricating high-quality epi-graphene through the so-called polymer-assisted sublimation growth (PASG) method in combination with specific surface pretreatment procedures.<sup>[32]</sup> Over a wide doping range, the quality of the graphene-based Hall devices was verified by the high electron mobilities and by accurate reproduction of the quantized Hall resistance (QHR) value, the von Klitzing constant  $R_K$ , in precision measurements. The fabricated doping series reveals a correlation between the onset of the QH plateau and the carrier density, which provides a reliable selection criterion for graphene-based devices for quantum resistance standards for the first time. The presented concentration-dependent F4-TCNQ doping technique also qualifies for other types of epitaxial graphene functionalization requirements for broader device applications.

## 2. Experimental Results and Discussion

### 2.1. Concentration-Dependent F4-TCNQ Molecular Doping of Epitaxial Graphene

The monolayer graphene samples were grown by PASG on 6H-SiC substrates.<sup>[32]</sup> A typical ultra-smooth, bilayer-free graphene

layer is shown in the atomic force microscopy (AFM) image in Figure 1a. The graphene surface was protected by a thin PdAu/Au layer during the device fabrication process. After microfabrication and removal of the protection layer the surface was cleaned by two different annealing procedures. One sample set was cleaned by vacuum annealing at 450 °C, and the other one was additionally annealed in a hydrogen atmosphere. After the annealing treatments, the different types of doping layer stacks were deposited on the graphene Hall bar. Finally, the Hall bar chips were mounted and wire-bonded in a sample holder, as shown in the photograph in Figure 1b.

Three different types of doping layer stacks were tested. For the investigation of the F4-TCNQ concentration dependence a 5-layer (5L) doping stack sequence was used which consists of two F4-TCNQ doping layers separated by two spacer layers and a cap layer (each  $\approx 100$  nm thickness), as sketched in Figure 1d. Four different doping concentrations with volume mixing ratios of F4-TCNQ/anisole to PMMA of 1%, 5%, 25%, and 50% were applied. Moreover, we fabricated two sets of samples with a single F4-TCNQ doping layer to investigate the robustness of the resistance quantization in the doped graphene layer against modifications of the multilayer doping structure. The 3-layer (3L) structure including a spacer layer and the 2-layer (2L) structure without a spacer between graphene and the F4-TCNQ doping layer are sketched in Figure 1e,f, respectively.

All graphene devices were characterized by magnetotransport measurements at a low temperature of 4.2 K. Longitudinal and Hall resistance  $R_{xx}$  and  $R_{xy}$  were measured as depicted in Figure 1

**Table 1.** Characteristics of the graphene Hall bar devices. F4-TCNQ concentrations, pre-treatment of the graphene surface, and type of doping-layer stack. One device was post-annealed at 150 °C for 11 h in a helium atmosphere after the first measurement. Charge carrier density, mobility, and sheet resistance were determined from measurements of the Hall and longitudinal resistance,  $R_{xy}$  and  $R_{xx}$ , on Hall bar devices at 4.2 K.

Volume ratio of F4-TCNQ /anisole to PMMA	Pre-annealing	Doping stack	Electron density [ $\text{cm}^{-2}$ ]	Mobility [ $\text{cm}^2 \text{V}^{-1} \text{s}^{-1}$ ]
0:100	no	1L copolymer	$2.40 \times 10^{11}$	6670
50:100	no	5L	$-1.96 \times 10^{10}$	17280
0:100	vacuum	1L copolymer	$5.83 \times 10^{11}$	5010
1:100	vacuum	5L	$3.61 \times 10^{11}$	7280
5:100	vacuum	5L	$2.22 \times 10^{11}$	8260
25:100	vacuum	5L	$9.83 \times 10^{10}$	8880
50:100	vacuum	5L	$6.69 \times 10^9$	48090
same device, post-annealed			$9.26 \times 10^{10}$	9970
0:100	H <sub>2</sub>	1L copolymer	$7.12 \times 10^{11}$	4290
1:100	H <sub>2</sub>	5L	$5.32 \times 10^{11}$	6290
5:100	H <sub>2</sub>	5L	$2.70 \times 10^{11}$	4520
50:100	H <sub>2</sub>	5L	$3.17 \times 10^{10}$	24240
5:100	vacuum	3L	$5.40 \times 10^{11}$	6680
5:100	H <sub>2</sub>	3L	$4.29 \times 10^{11}$	4390
50:100	vacuum	2L	$2.32 \times 10^{11}$	4260
50:100	vacuum	2L	$2.70 \times 10^{11}$	6640

c. The zero field ( $B = 0$ ) carrier density  $n$  was calculated from the initial slope of the Hall resistance curve  $R_{xy}(B)$ , by means of the classical Hall equation  $n = \Delta B / (e \cdot \Delta R_{xy})$  with the elementary charge  $e$ . The Hall mobility  $\mu = 1 / (e \cdot n \cdot \rho_{xx})$  was extracted from the zero-field resistivity value  $\rho_{xx}$  supposing the Drude transport model. The data of all devices are summarized in **Table 1**.

Three reference devices were fabricated to determine the initial carrier density of the undoped graphene layers (0:100 volume ratio of F4-TCNQ/anisole to PMMA) denoted as 1 layer (1L) copolymer in **Table 1**. After the removal of the PdAu/Au protection layer, one device was left untreated before coating with the copolymer. The resulting very low electron density ( $2.4 \times 10^{11} \text{ cm}^{-2}$ ) is not long-term stable which is a known behavior related to the surface protection layer and the acid-based removal process.<sup>[9]</sup> The other two reference devices were vacuum and hydrogen annealed, respectively, as described above. The higher electron densities of the annealed devices compared to those without annealing are attributed to the removal of ambient-related acceptor molecules from the graphene surface. The best cleaning is achieved by annealing in hydrogen atmosphere, resulting in the highest electron density.<sup>[33,34]</sup> One device (50% doping ratio, vacuum annealed, 5L) was post-annealed at 150 °C for 11 h in helium atmosphere after magnetotransport measurement (denoted post-annealed) that resulted in an electron density increase compared to the initial state (of  $6.69 \times 10^9$  to  $9.26 \times 10^{10} \text{ cm}^{-2}$ ).<sup>[28]</sup>

## 2.2. Magnetotransport Measurements

The change of the electronic properties by variation of the F4-TCNQ concentration was investigated by standard low-temperature magnetotransport measurements. The Hall resis-

tance curves  $R_{xy}$  and the longitudinal resistivity  $\rho_{xx}$  of the devices with 5L doping structures on vacuum pre-annealed graphene surfaces are exemplarily plotted in **Figure 2a,b**, respectively. The measurements show all features of a successful doping and a common trend for increasing doping concentration, namely a reduction of the  $n$ -type charge carrier density, see **Table 1**, which becomes visible by the steeper  $R_{xy}$  slopes around zero magnetic field. The electron concentration decreases gradually from the initial value  $n = 5.8 \times 10^{11} \text{ cm}^{-2}$  of the undoped graphene device to  $n = 6.7 \times 10^9 \text{ cm}^{-2}$  with increasing F4-TCNQ doping concentration. This result underlines the compensating character of the molecular acceptor F4-TCNQ.

The reduction of the electron density goes along with an increase of the electron mobility  $\mu$  which is a typical behavior for epi-graphene.<sup>[7–9,28,33,36]</sup> Values up to  $\mu = 48100 \text{ cm}^2 \text{V}^{-1} \text{s}^{-1}$  were obtained for the highest doping levels in agreement with literature values and underlines the high quality of the molecular doped graphene devices.<sup>[7,28,33]</sup> Interestingly, the mobility increase results in an increasing compensation level (higher F4-TCNQ concentration), indicating no severe degradation of the graphene transport properties by the molecular doping.

Fully developed quantum Hall resistance plateaus of  $R_{xy} \approx 12.9 \text{ k}\Omega$  related to the filling factor of  $\nu = 2$  are observed at high magnetic fields, see **Figure 2a**. With an increasing doping concentration, the onset of the plateaus gradually shifts to lower magnetic fields. For the highest doping level (50% F4-TCNQ volume mixing ratio) an onset at  $\approx 0.2 \text{ T}$  is observed (inset of

**Figure 2a**). For an exact determination of the onset of the quantized regime with sufficient quality for resistance metrology precision measurements are necessary as shown later. The shallow bump at the onset of the  $R_{xy}$  plateau is related to variations of the Hall angle, leading to small contributions of the longitudinal

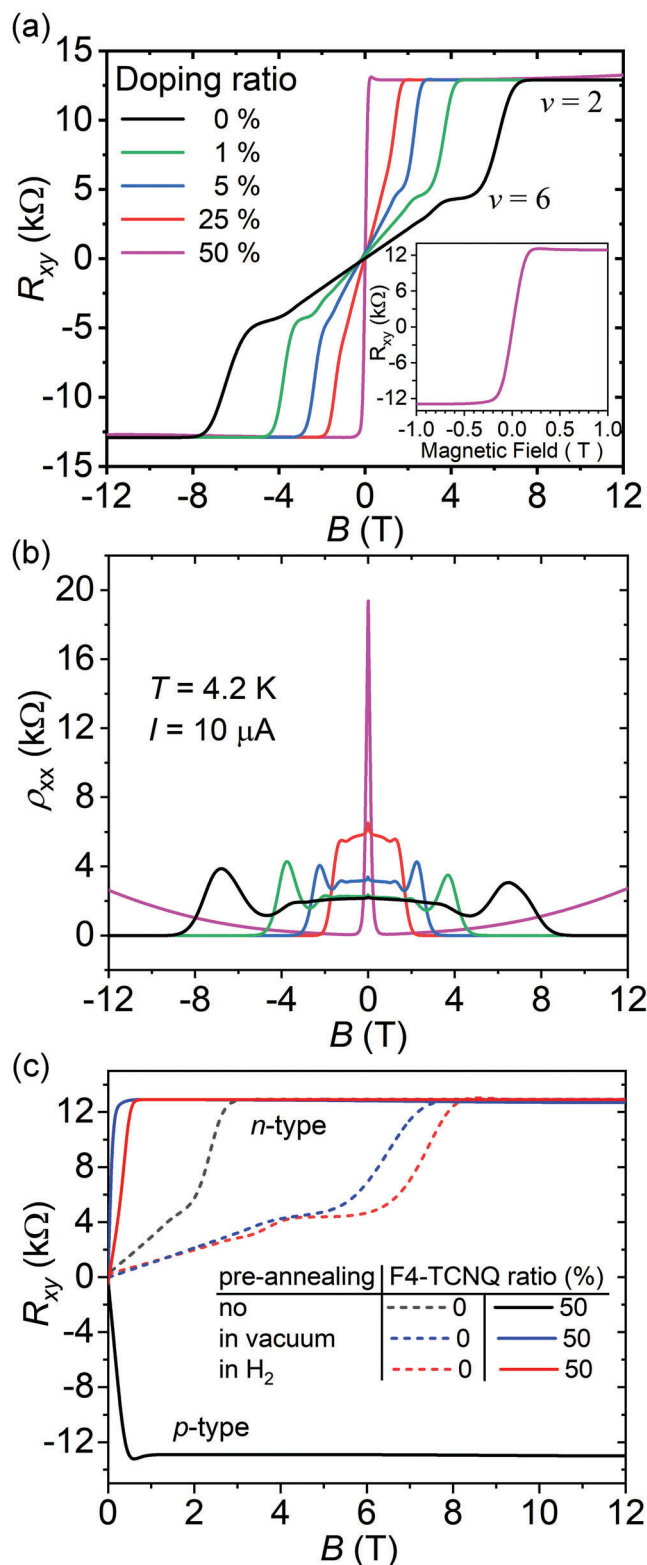


**Figure 2.** a) Standard Hall resistance measurements of the graphene-based Hall devices with different F4-TCNQ doping mixing ratios (5L doping stack) and one undoped device. The graphene surface was cleaned by vacuum annealing. The measurements show a gradual shift of the onset of the Hall plateau with an increasing doping level. The inset shows the low magnetic field range of the device with 50% doping ratio and the resistance

resistance. Despite the relatively high measurement temperature of 4.2 K, the higher-order  $\nu = 6$  plateau is well developed for the undoped and weakly doped devices.

The shift of the Hall plateau with increasing doping concentration is confirmed by the longitudinal resistivity  $\rho_{xx}$  measurements in Figure 2b that show a corresponding shift for the onset of the quantized regime with  $\rho_{xx} \approx 0$ . Moreover, the very symmetric  $B$ -field dependence of the  $\rho_{xx}$  and  $R_{xy}$  curves in both the magnetic field directions indicates a highly uniform carrier density distribution for the different F4-TCNQ doping concentrations in combination with PASG graphene.

Note, that, the sample with the highest doping level (50% ratio) and lowest carrier density does not exhibit a flat  $\rho_{xx}$  minimum and correspondingly deviates from the quantized  $R_{xy}$  value. The deviation from full quantization is indicated by the substantial increase of the longitudinal resistance following the onset of the Hall plateau at  $\approx 0.2$  T, and it is symmetric for both magnetic field directions. This resistance increase is a direct consequence of an incomplete filling of the 0th Landau band due to the low charge carrier density.<sup>[37]</sup>

### 2.3. Decisive Influence of Graphene's Initial Charge Carrier Density

For an exact adjustment of the carrier density by the concentration-dependent doping technique, a reliable and reproducible doping procedure is necessary. The initial carrier density of the as-grown graphene layer is equally important since doping with the F4-TCNQ acceptor is a compensation doping technique. The final carrier density of the doped graphene is determined by the initial value of the undoped graphene reduced by the density of carriers that are removed from the graphene by the compensation with F4-TCNQ acceptors. This is clearly observed in our experiments. When the same F4-TCNQ concentration (50:100) is applied to graphene with different pre-conditioning, and it becomes evident in magnetotransport measurements in Figure 2c. The same F4-TCNQ doping concentration leads to a shift of the Hall plateau to lower magnetic fields in case of the vacuum and the hydrogen pre-annealed graphene and to an increase of the initial Hall slope compared to the undoped (pristine) graphene. It is clearly visible that the electron density of the vacuum pre-annealed device with a lower initial value shifts to a lower final value (from  $n = 5.83 \times 10^{11}$  to  $6.69 \times 10^9 \text{ cm}^{-2}$ ) compared to the hydrogen annealed one, which shifts from a higher value of  $n = 7.12 \times 10^{11} \text{ cm}^{-2}$  to a higher final value of  $3.17 \times 10^{10} \text{ cm}^{-2}$ . This manifests in a steeper Hall slope and an onset of the Hall plateau at lower magnetic fields. The undoped device without treatment exhibits the lowest initial electron density ( $2.4 \times 10^{11} \text{ cm}^{-2}$ ) and the same F4-TCNQ doping concentration even leads to a complete compensation of

plateau starting at  $\approx 0.25$  T. The shallow bump is attributed to longitudinal resistance contributions at non-ideal Hall angles. b) Measurements of the longitudinal resistivity  $\rho_{xx}$  of the same device set. c) Comparison of the Hall resistances for differently pre-conditioned graphene devices without and with 50% volume ratio F4-TCNQ doping. The doping-related shift of the Hall curves indicates the decisive influence of the starting graphene properties on those of the finished doped device.

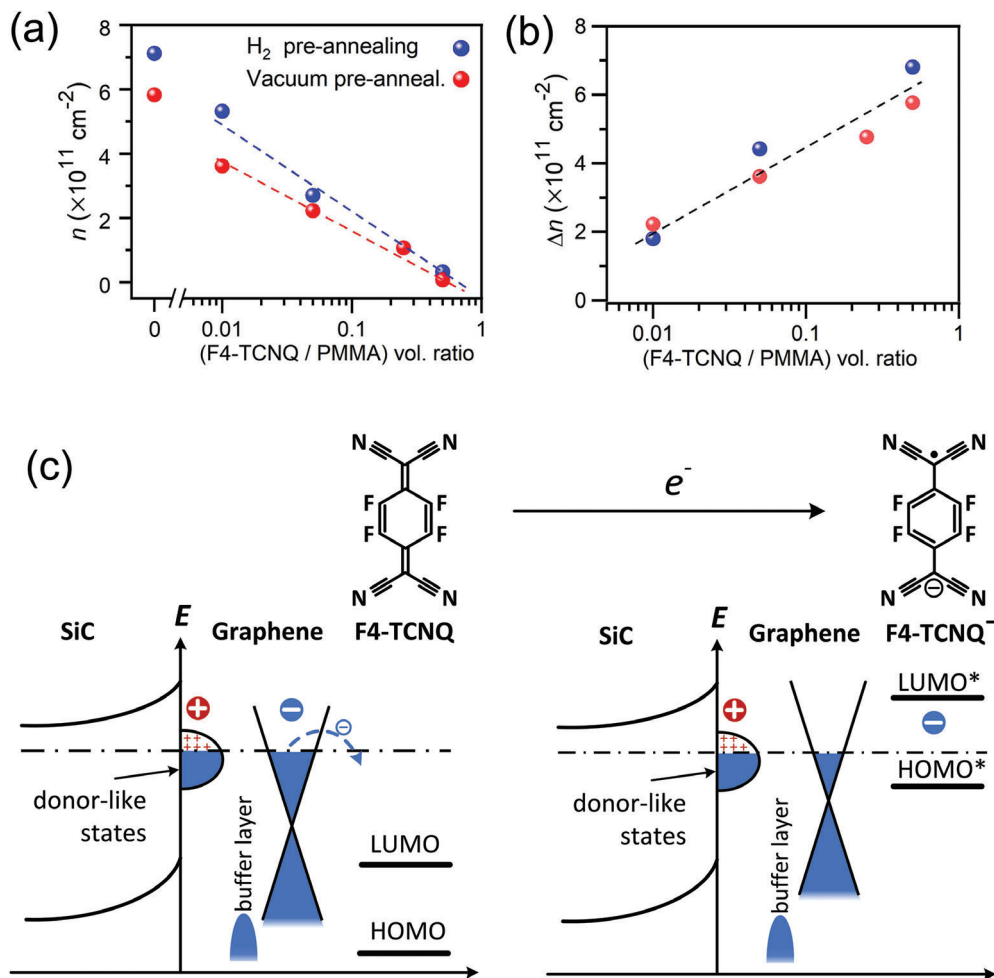


**Figure 3.** a) The electron density  $n$  of the F4-TCNQ doped graphene Hall bar devices (5L doping stack) is a function of the F4-TCNQ/anisole volume concentration in PMMA for both sample sets (graphene pre-annealing in vacuum and in hydrogen atmosphere). The differences at weak doping levels between both sample sets indicate the impact of the different initial carrier densities of the undoped graphene. b) The compensated carrier density,  $\Delta n = n_{\text{undoped}} - n_{\text{doped}}$ , by the F4-TCNQ charge transfer doping shows a sublinear increase as a function of the F4-TCNQ volume concentration. c) Schematic band diagram sketch for molecular doping of epitaxial graphene by F4-TCNQ. Left diagram: Before charge transfer, the high electron density of epitaxial graphene is attributed to donor-like states between the SiC surface and the buffer layer, e.g., Si dangling bonds. The neutral F4-TCNQ molecules near the graphene surface act as strong electron acceptors indicated by the energy position of the highest occupied molecular orbital (HOMO) and lowest unoccupied molecular orbital (LUMO) state which causes electron transfer from the graphene layer to the F4-TCNQ molecules. Right diagram: In the final doped state the electron concentration in the graphene layer is reduced, and the F4-TCNQ<sup>-</sup> charge transfer complex is formed. The excited HOMO\* and LUMO\* states shift to higher energies. The increasing negative charge accumulation above the graphene layer at higher doping levels leads to a gating effect and a self-limitation of the doping process. The chemical structures show a neutral F4-TCNQ molecule (left) and the anion F4-TCNQ<sup>-</sup> (right) after accepting one electron. By this reaction a delocalized ionic state is formed and the F4-TCNQ turns into an aromatic molecule.<sup>[35]</sup>

the electron density and a hole concentration of  $1.96 \times 10^{10} \text{ cm}^{-2}$  that becomes obvious by the inverse Hall curve in Figure 2c. This comparison shows that graphene pre-treatment and the knowledge of the initial carrier density are essential parameters for controlling the final carrier density of an F4-TCNQ-doped device.

It is worth mentioning that the presented F4-TCNQ doping technique allows the fabrication of high-quality *p*-type epitaxial graphene suitable for metrological applications.<sup>[22]</sup> This is in contrast to other studies in which no *p*-type doping could be achieved by direct evaporation of the molecular dopant on the graphene surface.<sup>[24–26,38]</sup> The reason is not clear, and it might be related to different initial electron densities or host matrix-related effects.

#### 2.4. Doping Model for F4-TCNQ molecular doped epitaxial graphene on SiC

The magnetotransport measurements of the graphene devices indicate that the electronic properties, in particular the electron density and the shift of the onset of the Hall plateau, are correlated with the degree of compensation given by the F4-TCNQ acceptor concentration. This decrease of  $n$  is depicted in Figure 3a for both sample sets of vacuum and hydrogen pre-annealed graphene devices with a 5L doping structure. The data show that a gradual reduction of the electron density over about two orders of magnitude can be achieved by increasing the doping

ratio up to 50%. This indicates a high reproducibility of the concentration-dependent doping technique and thus offers a new way for a reliable and easy tuning of the carrier density of epitaxial graphene. The difference in low doping ratios between both sample sets is attributed to the different initial carrier densities. This underlines the importance of a careful preparation of the graphene surface to obtain reproducible starting conditions.

The semi-logarithmic plot of the data in Figure 3a suggests a sublinear decrease of the carrier density in the graphene layer with increasing F4-TCNQ volume concentration. It shows the high effectiveness of this molecular dopant at small dopant concentrations but a moderation of the doping effect for higher F4-TCNQ concentrations. This becomes evident by the estimation of the compensated electron densities which is the difference between the values of the doped and the undoped samples,  $\Delta n = n_{\text{undoped}} - n_{\text{doped}}$ . Again, the corresponding plot in Figure 3b suggests a logarithmic increase of  $\Delta n$ , i.e. a sublinear behavior of the electron transfer as a function of the F4-TCNQ volume concentration that agrees well with the estimated low doping efficiency of F4-TCNQ on graphene.<sup>[28,39]</sup> Moreover, the sublinear behavior indicates a self-limiting effect with increasing doping concentration.

For the interpretation of this result, more detailed knowledge of the microscopic doping mechanism is needed. According to recent results, molecular doping is mediated by diffusion of the F4-TCNQ molecules from the doping layer through the copolymer spacer layer to the graphene surface.<sup>[28]</sup> The F4-TCNQ amount on the graphene surface is proportional to the concentration in the doping layer as given by the diffusion law.<sup>[28]</sup> Moreover, it can be assumed that the F4-TCNQ doping layer concentration is approximately proportional to the volume concentration in the doping solution since anisole completely evaporates during the 160°C annealing steps. Therefore, the F4-TCNQ concentration at the graphene surface is assumed to vary linearly with the F4-TCNQ volume ratio (abscissa in Figure 3a,b).

In the actual doping process, only dopant molecules close to the graphene surface are involved.<sup>[25]</sup> Density functional theory (DFT) calculations suggest a nearly parallel to the graphene surface-oriented F4-TCNQ molecules at a distance of a few angstroms.<sup>[26]</sup> In the charge transfer effects between the adsorbed F4-TCNQ and graphene, the cyano (CN) groups of the F4-TCNQ molecule play a crucial role, leading to the accumulation of charge carriers in their local environment in graphene (Figure S2, Supporting Information). The wavefunction overlap of  $\pi$ -bonds of graphene and F4-TCNQ results in the formation of charge-transfer complexes (CTC), and due to the strong electron affinity of F4-TCNQ (5.3 eV compared to 4.3 eV of epitaxial graphene), electrons at the Fermi level of graphene are transferred to the energetically lowest unoccupied molecular orbital (LUMO) state of the F4-TCNQ molecules, see Figure 3c.<sup>[25,26,39,40]</sup> Although the molecule can take up to two charged states,<sup>[41]</sup> only the single ionized anion (F4-TCNQ<sup>-</sup>) was experimentally observed.<sup>[25]</sup> Simulation results estimated an average charge transfer of about 0.3 – 0.4 electrons per F4-TCNQ molecule on the graphene surface.<sup>[26,39]</sup> This low value is confirmed by our first-principle DFT calculations that also predict a high energy but probably unstable double ionized F4-TCNQ state (Figure S3, Supporting Information). The amount of charge transfer from

graphene to the F4-TCNQ is controlled by two parameters: the number of available acceptors, and the difference in the work functions between graphene and the F4-TCNQ LUMO level.<sup>[7,42]</sup> In this picture the observed self-limitation of the doping process can be explained by a reduction of the work function of graphene and available sites for the F4-TCNQ molecule close to the graphene surface with increasing F4-TCNQ concentration. Furthermore, the transferred charge in the ionized F4-TCNQ<sup>-</sup> molecule is effectively insulated to the PMMA matrix since no further charge can be transferred to the PMMA due to the large energetic gap ( $\Delta E \approx 3.4$  eV) between the excited state of the F4-TCNQ<sup>-</sup> and the LUMO states of the ambient PMMA matrix (Figure S4, Supporting Information).

In a more realistic model, also the donor-like states (the origin of the high electron concentration of epitaxial graphene) at the interface between the SiC substrate and the buffer layer have to be taken into account, see Figure 3c.<sup>[43]</sup> They act as an electron reservoir that are donating electrons to the graphene, and it is assumed that their charge state also changes during the charge transfer equilibration process. This means that F4-TCNQ molecules on the graphene surface partially compensate electrons from the reservoir due to the energy difference between the LUMO of F4-TCNQ and the donor-like states as described by a general graphene doping model.<sup>[44]</sup>

In the schematic band diagram of Figure 3c the excited highest occupied molecular orbital (HOMO\*) level of the F4-TCNQ anions is sketched that have accepted an electron from the graphene layer. The increasing anion accumulation on top of the graphene sheet can be regarded as a negatively charged gate, and the Coulomb repulsion of electrons limits the electron transfer to the dopant molecules. This effect must also be considered in a more detailed description of the doping mechanism in analogy to the photo-chemical gating by light-induced acceptors in a resist layer on top of epitaxial graphene.<sup>[7]</sup>

The data of the 3L and 2L structures are not plotted together with the 5L ones in Figure 3a,b because of the unequal diffusion behavior of the different layer sequences. However, when comparing the electron densities, a consistent picture is obtained. The 3L structures show a higher carrier density compared to 5L with the same F4-TCNQ doping ratio (5:100). This is attributed to a lower F4-TCNQ supply from only one doping layer that results in a weaker compensation and finally in a higher electron concentration in the 3L structures. A larger loss of the molecular dopant by out-diffusion to the surface could be another reason for the weaker doping strength of the 3L structure.

The 2L structures show a lower electron density than 3L. This is reasonable since the doping volume ratio used for the 2L structures is 10 times higher. The comparison of the 5L and 2L structures (with and without spacer layer, respectively) for the same doping ratio (50:100) shows a more than 10 times lower electron concentration than the 5L structure. However, it is difficult to estimate the influence of the missing spacer layer since the effect of the missing second doping layer cannot be assessed as discussed above.

It is interesting to note that the 2L- and the 3L- stack devices show mobility values comparable to the one with 5L-stacks. This shows that the doping stack variation and the missing copolymer spacer layer have no fundamental effect on the scattering of conducting electrons in the graphene layer.

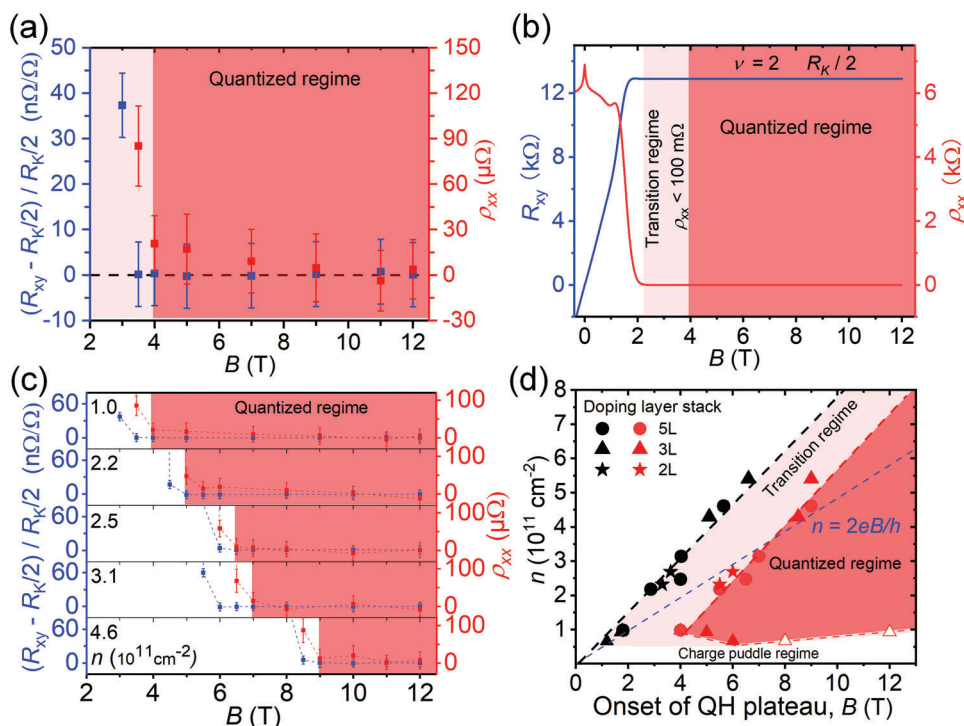


**Figure 4.** a) Precision measurement of Hall resistance and longitudinal resistivity with the CCC resistance bridge at 4.2 K and  $I = 38 \mu\text{A}$  of the vacuum annealed device with 25% volume concentration F4-TCNQ (5L doping stack). The quantized regime is defined as the magnetic field at which  $\rho_{xx} = 0$  within the uncertainty which is  $\pm 23 \mu\Omega$  ( $k = 2$ ) for this device. Here, the onset of the quantized regime is at  $B = 4$  T. Relative deviation of the Hall resistance from the nominal value is  $|(R_{xy} - R_K/2) / (R_K/2)| < (0.7 \pm 7.1) \times 10^{-9}$  in the plateau range  $B = 4 - 12$  T. b) The apparent onset of the Hall plateau observed in a standard (non-precision) magnetotransport measurement appears at a lower magnetic field. We define the onset of this transition region when the resistivity  $\rho_{xx} < 100 \text{ m}\Omega$  which is at  $B = 2$  T for this device. c) Precision measurements of Hall and longitudinal resistance at 4.2 K and  $I = 38 \mu\text{A}$  of five F4-TCNQ doped devices (5L doping stack) ordered according to their electron density. The quantized regime ( $\rho_{xx} \leq 50 \mu\Omega \pm 23 \mu\Omega$ ) is marked in red. The onset of the quantized regime shifts with higher electron density to higher magnetic fields. In the quantum regime the relative deviation of the QH resistance from the nominal value is  $< (0.7 \pm 5) \times 10^{-9}$ . The uncertainties are combined, expanded uncertainties ( $k = 2$ ) and thus include the uncertainties attached to the reference resistor. d) Onset of the quantum Hall plateaus as a function of the (zero field) electron density  $n$  of the devices with a 5L doping stack evaluated from the precision measurements in (c) and five other F4-TCNQ doped graphene devices with 3L- and 2L-doping stacks fabricated and evaluated in the same way. The strong correlation between the electron density of the devices and the onset of the Hall plateau for the transition and the quantized region is a valuable criterion for the selection of graphene devices in quantum metrology. The open symbols mark the end of the QH plateau. The blue dashed line represents the carrier density for the filling factor  $\nu = 2$  in the absence of charge transfer.

## 2.5. Precision Measurements of the Quantum Hall Resistance

Precision measurements of the QHR are a very sensitive tool to obtain information about the quality of the graphene device and the homogeneity of the carrier distribution. In combination with the presented doping series, the impact of dopant concentration variation on the transport properties of epitaxial graphene can be studied for the first time. This opens a unique opportunity in quantum resistance metrology to systematically investigate the quantization at lower carrier densities and Hall resistance plateaus at lower magnetic fields.

Since for advanced quantum resistance metrology applications, graphene devices can be used in much relaxed conditions, precision QHR measurements were performed at constant magnetic flux density values  $B$  from 3 to 12 T (maximum accessible magnetic field range in our setup) and at a temperature of 4.2 K. **Figure 4a** shows the result of the graphene device, which was vacuum annealed and doped by a volume ratio of 25%. Displayed is the relative deviation of the measured resistance values from the nominal quantized value at filling factor  $\nu = 2$ ,  $\Delta R_{xy} / (R_K/2) =$

$(R_{xy} - R_K/2) / (R_K/2)$  and the longitudinal resistivity values  $\rho_{xx}$  as a function of the magnetic flux density  $B$ . The Hall resistance exhibits a perfect quantization of  $|\Delta R_{xy} / R_K/2| < (0.7 \pm 7.1) \times 10^{-9}$  with no significant deviation from the nominal value  $R_K/2$  for magnetic fields  $\geq 3.5$  T. The  $\rho_{xx}$  value of  $80 \mu\Omega$  at  $B = 3.5$  T has no detrimental effect on the QHR value due to the very small Hall angle ( $s$  parameter). At 4 T the longitudinal resistivity drops to  $(20.1 \pm 23.0) \mu\Omega$  and further on to  $(3.8 \pm 19.7) \mu\Omega$  at 12 T, demonstrating zero longitudinal resistivity within the uncertainty and a dissipationless state in the graphene's electron gas. The measured  $\rho_{xx}$  value at  $B = 4$  T is lower than typically published values obtained at 4.2 K.<sup>[31,45]</sup> The vanishing of the longitudinal resistivity within the uncertainty of  $\pm 23 \mu\Omega$  at  $B \geq 4$  T and at  $T = 4.2$  K is an excellent criterion for the quantization of the device. It indicates a homogenous carrier distribution and spatial dispersion of the compensating dopant molecules. The vanishing resistivity also proves that no parallel transport channel has formed even for the highest doping concentration.

The comparison of the precision and the standard magnetotransport QHR measurements (as shown in Figure 2a,b) exhibits

a notable difference in the onset of the QH plateau for the same devices that originates from the different resolution of both measurements. This is depicted in Figure 4b, which shows the standard QHR measurement of the same device as in Figure 4a. The onset of the apparent plateau in the standard QHR measurement (Figure 2b) marks the beginning of the so-called transition regime in which the transport behavior switches from dissipative transport to the QH regime. The onset, as well as the width of this regime, is determined by different disorder types and spatial inhomogeneities. For further evaluation, we define the start of the transition regime as the  $B$  value when  $\rho_{xx}$  drops below 100 m $\Omega$ . For this device, the transition regime starts at  $\approx 2$  T, which is  $\approx 2$  T lower than the onset of the quantized regime.

Precision measurements of all doped devices were performed, and the QH plateau regions of  $\Delta R_{xy}$  and  $\rho_{xx}$  are plotted in Figure 4c, with respect to their carrier density  $n$ . The plots show that the onset of the quantized Hall plateau shifts to higher magnetic fields with increasing electron density. The vanishing of the longitudinal resistivity within the uncertainty is a reliable criterion to determine the onset of the quantized regime since the deviation of the QHR reaches a  $10^{-9}$  accuracy already at somewhat lower magnetic fields (see Figure 4a). The magnetic field values of the onset of the transition regime and the quantized regime were determined for all doped devices and are plotted in Figure 4d together with the corresponding electron density. This plot displays the correlation between the electron density of the device and the minimal magnetic field at which accurate quantization is achieved. It is a valuable selection criterion for graphene QH devices that are used as resistance standards since the quantized regime identifies the regime in which devices are typically used for resistance calibrations. Although the shift of the Hall plateau is a general behavior that is related to the elementary correlation of the applied magnetic field and the non-constant carrier density, the extraordinary broad Hall plateau of epitaxial graphene prevents the determination of the plateau center for this material.<sup>[37,46]</sup> Therefore, it is of high practical benefit for the application of graphene-based quantum Hall devices to define an accessible characteristic parameter that describes the Hall plateau. From the data plot in Figure 4d, a width of the transition regime of about 2 – 3 T is estimated. By further reducing the disorder in epitaxial graphene, we expect that the regime of accurate resistance quantization can be achieved at even lower magnetic fields.

The observed correlation between (zero field) carrier density and the onset value of the QH plateau in Figure 4d is valid for the 5L doping stacks over a wide range of electron densities of one order of magnitude. Additionally, the onset values of the 3L and the 2L devices were evaluated in the same way from the respective precision QH measurements. The data in Figure 4d show that the performance and characteristics of all devices is very similar despite the different doping layer structures (2L, 3L, 5L). This result indicates that the observed characteristics are typical for state-of-the-art monolayer epitaxial graphene devices that are doped with the molecular dopant F4-TCNQ embedded in a PMMA resist matrix. In practice, inhomogeneities of any type (e.g., poorer structural graphene quality or inhomogeneous doping) can change the behavior and shift the onset of the quantized regime to higher magnetic field values.

For the devices of this study, Figure 4d shows that  $n = 1 \times 10^{11} \text{ cm}^{-2}$  is the lowest electron density that allows precise resistance calibration at magnetic fields from 4 T to values of at least 12 T. For a slightly lower density of  $9.3 \times 10^{10} \text{ cm}^{-2}$ , a finite QH plateau is observed spanning from 5 to 12 T. For further reduced electron density the plateau width is continuously shrinking and for  $n = 6.7 \times 10^{10} \text{ cm}^{-2}$  it spans from 6 to 8 T. (The plateau ends are marked by open symbols in Figure 4d.) The shrinking QH plateau is attributed to two effects. The delayed onset of the QH plateau shows the stronger impact of disorder at lower electron densities. Whereas the termination of the quantized regime (non-zero longitudinal resistivity) is attributed to an incomplete filling of the Landau level due to the low carrier density in graphene. This is a clear indication that the charge transfer from doner-like states to graphene is not constant but is smaller for devices with a lower zero-field carrier density compared to those with higher one. This is in good agreement with an estimate for the maximum transferable charge in the charge transfer model.<sup>[37]</sup> The highly doped device with the lowest density of  $n = 6.69 \times 10^9 \text{ cm}^{-2}$  showed no quantized regime, which becomes clear already from the non-zero resistivity minimum of the standard QHR measurement in Figure 2b. At such low electron densities below  $1 \times 10^{11} \text{ cm}^{-2}$  the graphene device is in the charge puddle regime. The related disorder due to inhomogeneous charge distribution and coexisting electron and hole puddles deteriorates the Hall quantization and inhibits metrological applications.<sup>[37,47,48]</sup>

Note, that Figure 4d shows the relation between the onset of the quantized regime and the zero field ( $B = 0$ ) electron density. Inside the QH plateaus, the actual, higher electron density has to be considered, including the field-dependent charge transfer from the donor-like states into the Landau level as described by the charge transfer model.<sup>[37,46,49]</sup> In the absence of charge transfer, the center position of a Hall plateau at filling factor  $\nu$  as a function of carrier density and magnetic field is described by the relation  $n = \nu eB/h$ . For an exact filling factor  $\nu = 2$  this relation is plotted for orientation as blue dashed line in Figure 4d. It determines the centers of the QH plateau of classical semiconductor, e.g., GaAs/AlGaAs, 2DEG devices with constant carrier density. In our epitaxial graphene devices, the center position of the Hall plateau at  $\nu = 2$  is shifted to a higher magnetic field (right side of the blue dashed line). From this, we can qualitatively deduce, that the true carrier density of graphene in the magnetic field is much higher than the zero-field carrier density. This is another evidence for the existence of a magnetic field-dependent charge transfer process in epitaxial graphene.

In an actual device, the onset of the quantized regime is determined by the magnitude of the disorder in the epitaxial graphene layer and by the measurement temperature. The onsets (Figure 4d) and their linear  $B$ -field dependence in the range of  $n > 1 \times 10^{11} \text{ cm}^{-2}$  are only valid for the chosen temperature and current of the magnetotransport measurements, in this case,  $T = 4.2$  K and  $I = 38 \mu\text{A}$ . A change of the thermal carrier distribution and current heating directly impact the longitudinal resistivity and the onset of the Hall resistance quantization. Further precision measurements of current and temperature dependence of the QHR exhibits accurate quantization within a few parts in  $10^9$  up to currents of 230  $\mu\text{A}$  (current limit of the CCC bridge) at

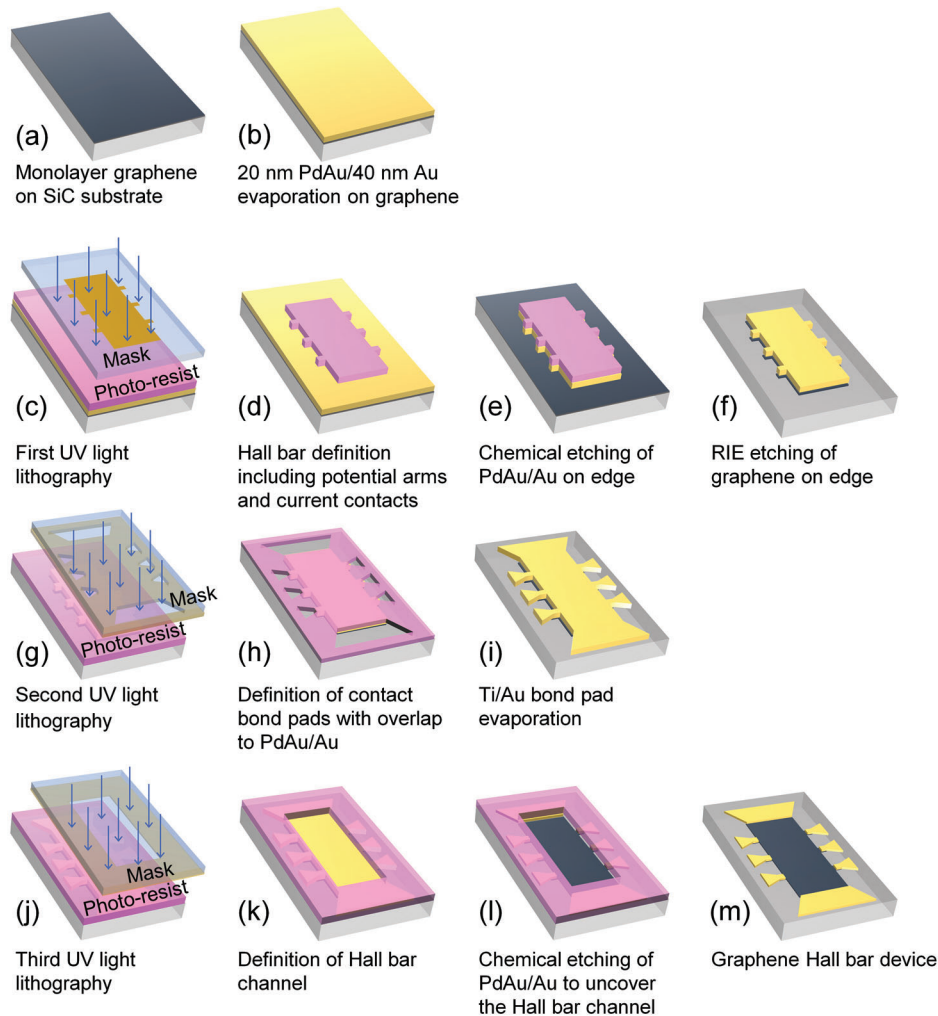


**Figure 5.** a) Monolayer epitaxial graphene on SiC substrate (5 mm × 10 mm). b) Thermal evaporation of 20 nm PdAu / 40 nm Au on the as-grown graphene surface. The precious metal layer prevents contact with organic resist during the microfabrication process. c–d) First UV lithography step for Hall bar definition by wet/dry etching. e) Chemical wet etching of the surrounding PdAu/Au layer on edge by  $\text{ACI}_2$ , while the Hall bar channel is protected by photo-resist. Afterwards the photo-resist was removed by acetone and isopropanol. f) RIE etching of the graphene on edge, while the graphene below the channel is protected. The Pd/Au layer forms the Ohmic contact to graphene at the potential arms and the current contact positions. The contact areas have a finger-like shape. g–h) Second UV lithography step for bond pad fabrication. i) The bond pads are formed by thermal evaporation of a 10 nm Ti and 100 nm Au layer, lift-off process on SiC and with overlap to the PdAu/Au layer at the potential arms and current contacts. j–k) Third UV lithography step for uncovering the graphene Hall bar channel. l) Removing of the PdAu/Au layer on the Hall bar channel by  $\text{ACI}_2$  wet-chemical etching. m) Removal of the photo-resist by acetone and isopropanol.

4.2 K,<sup>[50]</sup> which is in good agreement with the high QH breakdown currents measured in graphene devices.<sup>[31,45,49,51]</sup> Our temperature dependent precision measurements show a shift of the QH plateau (quantized regime) by  $\approx 1$  T to higher  $B$ -values for a temperature change of 2 K (from 2.2 to 4.2 K),<sup>[50]</sup> which is a typical result for epitaxial graphene.<sup>[31,45,49]</sup>

The excellent quantization of the Hall resistance at 4.2 K and 4 T simplifies the experimental measurement set-up in quantum metrology compared to 1.5 K and 10 T for conventional GaAs-based resistance standards. A further shift of the quantized Hall regimes to lower field values is desirable. For this, a further reduction of disorder, for instance by suppressing the formation of charge puddles at low carrier densities, is necessary.

### 3. Summary and Conclusion

Molecular doping of epitaxial graphene on SiC was performed by functionalization with the acceptor F4-TCNQ in three different types of multilayer sequences. The doping level was tuned by variation of the acceptor concentration in the initial PMMA/anisole solution and Hall measurements showed that the intrinsic high electron density of the epitaxial graphene layer could be successfully reduced to lower values. For the highest doping level, a shift of the Fermi level across the charge neutrality point into the  $p$ -type regime was observed. The results confirm that due to the nature of compensation doping, the initial graphene properties, as well as the concentration of the dopant, determine the final

carrier density. A low doping efficiency was found, showing a logarithmic decrease of the electron density on the F4-TCNQ dopant concentration. An F4-TCNQ doping model is presented, which explains the self-limiting doping behavior by geometrical and self-gating effects. Such produced Hall devices need no further treatment for carrier density tuning before the measurement. The high quality of the graphene-based devices was verified by precision quantum Hall resistance measurements of two concentration-dependent doping series. The data indicates a homogenous charge carrier distribution and dissipationless longitudinal magneto transport for all doping levels  $n > 1 \times 10^{11} \text{ cm}^{-2}$ . A clear correlation between the electron density of the graphene Hall devices and the onset of the quantized regime of the  $\nu = 2$  resistance plateau could be derived from the data. This turns out to be valuable for the selection of graphene devices in quantum resistance metrology. The observed correlation is independent of the used doping-layer stack sequence, 5L, 3L, and 2L, respectively. Our work represents the first detailed study of the concentration-dependent F4-TCNQ doping method and thus constitutes an essential building block for the design of future electronic device applications based on epitaxial graphene.

#### 4. Experimental Section

Monolayer graphene was grown on a semi-insulating 6H-SiC(0001) specimen ( $5 \times 10 \text{ mm}^2$ ) by means of the polymer-assisted sublimation growth (PASG) growth method.<sup>[32]</sup> The nominal miscut of the SiC wafer from II-VI Comp. was  $\approx -0.06^\circ$  toward [1–100] and almost zero toward [11–20].

The sequence of the Hall bar fabrication steps is displayed in **Figure 5**. The Hall bar fabrication started with the deposition of a precious metal layer (20 nm PdAu alloy (mass ratio of 60% Pd to 40% Au) + 40 nm Au) directly on the as-grown graphene surface to prevent contact with organic resist during the microfabrication process. Similar processes are described in the literature.<sup>[9,52]</sup> Graphene Hall bars were fabricated by optical lithography, reactive ion etching (RIE), thermal metal deposition, and wet etching (potassium iodide solution, MicroChemicals TechniEtch ACI2). The Hall bars are 1600  $\mu\text{m}$  long and 400  $\mu\text{m}$  wide, with six voltage probes that are separated by a distance of 400  $\mu\text{m}$  from each other, see **Figure 1b**. The geometry ratio of the Hall bar width to the distance between two neighboring contact pairs is 1:1 ( $w = 400 \mu\text{m}$ ,  $l = 400 \mu\text{m}$ ). The Hall bar is oriented almost perpendicular to the terrace steps. The bond pads on the SiC substrate were formed by a titanium (10 nm)/gold (100 nm) layer with small overlap to the PdAu/Au layer. The contact resistances of all devices were measured by three-terminal measurements at low temperatures (4.2 K) in the quantum Hall regime. The low values of  $< 1 \Omega$  guarantee reliable QHR measurements.

**Doping Layer Fabrication:** After microfabrication and removing the PdAu/Au protection layer from the graphene, the surface was cleaned by two different annealing procedures. For each treatment, the chamber was pumped to  $10^{-7}$  mbar for 12 h. One sample set was cleaned by annealing in vacuum at 450  $^\circ\text{C}$  for 2 h, and the other one was additionally annealed in a hydrogen atmosphere (1000 mbar) at 450  $^\circ\text{C}$  for another 2 h. After cooling down and immediately after opening of the vacuum chamber the different types of doping layer stacks were deposited on the graphene Hall bar via spin-coating, **Figure 1d–f**.

The molecular doping mixture was produced by dissolving 25 mg 2,3,5,6-Tetrafluoro-7,7,8,8-Tetracyanoquinodimethane (F4-TCNQ) powder (Sigma–Aldrich) in 3 mL anisole.<sup>[28]</sup> By subsequent dilution of a portion of this mixture in 950 K Polymethylmethacrylat (PMMA) (MicroChemicals) four different doping concentrations were obtained with volume mixing ratios of F4-TCNQ/anisole to PMMA of 1%, 5%, 25%, and 50%. The spacer and the cap layer were fabricated by using EL6 copolymer (MMA

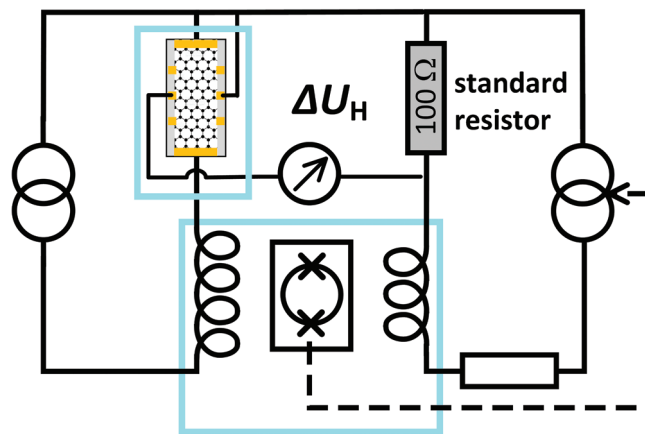


**Figure 6.** Schematic wiring diagram of the CCC resistance bridge used for the precision quantum Hall measurements. The voltage  $\Delta U_H$  is the difference between the Hall voltage of the QH device and the voltage across a 100  $\Omega$  reference resistor which was calibrated against the quantized value  $R_K/2$  of a conventional GaAs-quantum Hall resistance standard. The QH device and the CCC is cooled to cryogenic temperatures of 4.2 K. The 100  $\Omega$  resistor is kept at constant temperature close to room temperature. Uncertainties attached to the reference resistors are taken into account in the type B uncertainty of the resulting QH resistance values.

(8.5) MAA). The doping layer and the co-polymer spacer and cap layer, respectively, were deposited sequentially. Each layer was deposited by spin-coating and was annealed for 5 min at 160  $^\circ\text{C}$  (above the PMMA glassy temperature). Finally, the specimen was diced, and one Hall bar chip was mounted and wire-bonded in a TO-8 sample holder, as shown in the photograph in **Figure 1b**.

**Standard Magnetotransport and Precision Quantum Hall Resistance Measurements:** The magnetotransport measurements of the graphene QHR devices were performed in a commercial bath cryostat at 4.2 K with a superconducting magnet operating at fields up to 12 T. The standard magnetotransport measurements were performed with a Keithley 6220 current source and a Keithley 2182 Nanovoltmeter.

The precision measurements were performed using a commercial cryogenic current comparator (CCC) resistance bridge system from Magnicon GmbH. A schematic wiring diagram is shown in **Figure 6**. The Hall resistance  $R_{xy}$  of the graphene device was compared to a temperature controlled 100  $\Omega$  reference resistor which was calibrated against the quantized value  $R_K/2$  of a conventional GaAs-quantum Hall resistance standard. The balancing of the bridge was realized by compensation of the current-induced magnetic flux of both arms of the CCC bridge that was detected by a sensitive dc SQUID in a cryogenic environment. The remaining Hall voltage difference  $\Delta U_H$  is a direct measure of the deviation from  $R_K/2$  value. The deviations  $\Delta R_{xy} = (\Delta U_H / I - R_K / 2)$  from the nominal quantized value  $R_K/2$  were calculated.

The longitudinal resistances  $R_{xx}$  were determined by two individual resistance measurements using the CCC resistance bridge.  $R_{xx}$  is calculated as the difference of the Hall resistance of diagonal and opposite contact pairs.<sup>[53]</sup>

**Statistical Analysis of the Precision QHR Measurements:** In the case of the precision QHR measurements using the CCC resistance bridge, combined extended type A and type B uncertainties ( $k = 2$ ) were taken into account. The typical type A uncertainties of the bridge voltage difference is  $\leq 0.6$  nV for the typical total measurement time of 5 min with a sample count / number of measurement cycles of  $N = 12$ . The mean value and the standard deviation (Type A uncertainty) is calculated by the measurement bridge software. Typical combined uncertainties (type A and B) of the bridge are  $1.25 \text{ n}\Omega^{-1}$  ( $k = 1$ ) and combined expanded uncertainties of  $2.5 \text{ n}\Omega^{-1}$  ( $k = 2$ ). The main contribution to type B uncertainty arises from uncertainties attached to the 100  $\Omega$  reference resistor.<sup>[22]</sup>

The resulting combined expanded uncertainty of the longitudinal resistance was typically  $\approx 18 \mu\Omega$  for measurements inside the resistance plateau ( $R_{xx} \approx 0$ ) where the noise level was low. Each of the two individual Hall measurements that were needed to determine the longitudinal resistance was determined from  $N = 12$  samples/measurement cycles.

## Supporting Information

Supporting Information is available from the Wiley Online Library or from the author.

## Acknowledgements

This work was supported by the Joint Research Project GIQS (18SIB07). This project received funding from the European Metrology Programme for Innovation and Research (EMPIR) co-financed by the Participating States and from the European Unions' Horizon 2020 research and innovation programme. The authors also thank the Deutsche Forschungsgemeinschaft Research Unit FOR5242 for their support. This work was cofunded by the Deutsche Forschungsgemeinschaft (DFG, German Research Foundation) under Germany's Excellence Strategy – EXC-2123 QuantumFrontiers – 390837967.

## Conflict of Interest

The authors declare no conflict of interest.

## Data Availability Statement

The data that support the findings of this study are available from the corresponding author upon reasonable request.

## Keywords

epitaxial graphene on SiC, F4-TCNQ, graphene functionalization, molecular doping, quantum Hall resistance, quantum resistance metrology

Received: August 17, 2022  
Revised: September 29, 2022  
Published online:

- [1] M. Sprinkle, P. Soukiassian, W. A. de Heer, C. Berger, E. H. Conrad, *Phys. Status Solidi Rapid Res. Lett.* **2009**, *3*, A91.
- [2] M. Beshkova, L. Hultman, R. Yakimova, *Vacuum* **2016**, *128*, 186.
- [3] K. S. Novoselov, Z. Jiang, Y. Zhang, S. V. Morozov, H. L. Stormer, U. Zeitler, J. C. Maan, G. S. Boebinger, P. Kim, A. K. Geim, *Science* **2007**, *315*, 1379.
- [4] K. V. Emtsev, A. Bostwick, K. Horn, J. Jobst, G. L. Kellogg, L. Ley, J. L. McChesney, T. Ohta, S. A. Reshanov, J. Röhr, E. Rotenberg, A. K. Schmid, D. Waldmann, H. B. Weber, T. Seyller, *Nat. Mater.* **2009**, *8*, 203.
- [5] P. Willke, J. A. Amani, A. Sinterhauf, S. Thakur, T. Kotzott, T. Druga, S. Weikert, K. Maiti, H. Hofsä, M. Wenderoth, *Nano Lett.* **2015**, *15*, 5110.
- [6] T. Shen, J. J. Gu, M. Xu, Y. Q. Wu, M. L. Bolen, M. A. Capano, L. W. Engel, P. D. Ye, *Appl. Phys. Lett.* **2009**, *95*, 172105.
- [7] S. Lara-Avila, K. Moth-Poulsen, R. Yakimova, T. Bjørnholm, V. Fal'ko, A. Tzalenchuk, S. Kubatkin, *Adv. Mater.* **2011**, *23*, 878.
- [8] A. Lartsev, T. Yager, T. Bergsten, A. Tzalenchuk, T. J. B. M. Janssen, R. Yakimova, S. Lara-Avila, S. Kubatkin, *Appl. Phys. Lett.* **2014**, *105*, 10.
- [9] Y. Yang, L. I. Huang, Y. Fukuyama, F. H. Liu, M. A. Real, P. Barbara, C.-T. Liang, D. B. Newell, R. E. Elmquist, *Small* **2015**, *11*, 90.
- [10] T. Oe, A. F. Rigosi, M. Kruskopf, B.-Y. Wu, H.-Y. Lee, Y. Yang, R. E. Elmquist, N. Kaneko, D. G. Jarrett, *IEEE Trans. Instrum. Meas.* **2020**, *69*, 3103.
- [11] N. T. M. Tran, S. M. Mhatre, C. N. Santos, A. J. Bicch, M. L. Kelley, H. M. Hill, D. Saha, C.-T. Liang, R. E. Elmquist, D. B. Newell, B. Hackens, C. A. Hacker, A. F. Rigosi, *Carbon* **2022**, *197*, 350.
- [12] S. M. Mhatre, N. T. M. Tran, H. M. Hill, D. Saha, A. R. Hight Walker, C.-T. Liang, R. E. Elmquist, D. B. Newell, A. F. Rigosi, *Phys. Rev. B* **2022**, *105*, 205423.
- [13] A. Tadich, M. T. Edmonds, L. Ley, F. Fromm, Y. Smets, Z. Mazej, J. Riley, C. I. Pakes, T. Seyller, M. Wanke, *Appl. Phys. Lett.* **2013**, *102*, 241601.
- [14] E. Pallecchi, M. Ridene, D. Kazazis, C. Mathieu, F. Schopfer, W. Poirier, D. Mailly, A. Ouerghi, *Appl. Phys. Lett.* **2012**, *100*, 253109.
- [15] S. Novikov, N. Lebedeva, K. Pierz, A. Satrapinski, *IEEE Trans. Instrum. Meas.* **2015**, *64*, 1533.
- [16] I. Gierz, C. Riedl, U. Starke, C. R. Ast, K. Kern, *Nano Lett.* **2008**, *8*, 4603.
- [17] A. F. Rigosi, M. Kruskopf, H. M. Hill, H. Jin, B.-Y. Wu, P. E. Johnson, S. Zhang, M. Berilla, A. R. Hight Walker, C. A. Hacker, D. B. Newell, R. E. Elmquist, *Carbon* **2018**, *142*, 468.
- [18] J. A. Robinson, M. LaBella, K. A. Trumbull, X. Weng, R. Cavellero, T. Daniels, Z. Hughes, M. Hollander, M. Fanton, D. Snyder, *ACS Nano* **2010**, *4*, 2667.
- [19] J. Hu, A. F. Rigosi, M. Kruskopf, Y. Yang, B.-Y. Wu, J. Tian, A. R. Panna, H.-Y. Lee, S. U. Payagala, G. R. Jones, M. E. Kraft, D. G. Jarrett, K. Watanabe, T. Taniguchi, R. E. Elmquist, D. B. Newell, *Sci. Rep.* **2018**, *8*, 15018.
- [20] M. S. Bresnehan, M. J. Hollander, R. L. Marucci, M. LaBella, K. A. Trumbull, R. Cavellero, D. W. Snyder, J. A. Robinson, *Proc. SPIE* **2012**, *8462*, 846207.
- [21] E. Rigosi, C.-I. Liu, B. Y. Wu, H.-Y. Lee, M. Kruskopf, Y. Yang, H. M. Hill, J. Hu, E. G. Bittle, J. Obrzut, A. R. Hight Walker, R. E. Elmquist, D. B. Newell, *Microelectron Eng.* **2018**, *194*, 51.
- [22] J. Park, K.-G. Lim, D.-H. Chae, *Sci. Technol.* **2022**, *33*, 115019.
- [23] D.-H. Chae, M. Kruskopf, J. Kučera, J. Park, Y. Yin, P. Svoboda, P. Chrobok, F. Couëdo, N. T. M. Tran, D. B. Kim, K. Pierz, M. Gtz, F. Schopfer, *Meas. Sci. Technol.* **2022**, *33*, 065012.
- [24] W. Chen, S. Chen, C. Q. Dong, Y. G. Xing, A. T. S. Wee, *J. Am. Chem. Soc.* **2007**, *129*, 10418.
- [25] C. Coletti, C. Riedl, D. S. Lee, B. Krauss, L. Patthey, K. Von Klitzing, J. H. Smet, U. Starke, *Phys. Rev. B* **2010**, *81*, 235401.
- [26] J. T. Sun, Y. H. Lu, W. Chen, Y. P. Feng, A. T. S. Wee, *Phys. Rev. B* **2010**, *81*, 155403.
- [27] J. Jobst, D. Waldmann, F. Speck, R. Hirner, D. K. Maude, T. Seyller, H. B. Weber, *Phys. Rev. B* **2010**, *81*, 195434.
- [28] H. He, K. H. Kim, A. Danilov, D. Montemurro, L. Yu, Y. W. Park, F. Lombardi, T. Bauch, K. Moth-Poulsen, T. Iakimov, R. Yakimova, P. Malmberg, C. Müller, S. Kubatkin, S. Lara-Avila, *Nat. Commun.* **2018**, *9*, 3956.
- [29] H. He, S. Lara-Avila, K. H. Kim, N. Fletcher, S. Rozhko, T. Bergsten, G. Eklund, K. Cedergren, R. Yakimova, Y. W. Park, A. Tzalenchuk, S. Kubatkin, *Metrologia* **2019**, *56*, 045004.
- [30] M. Kruskopf, R. E. Elmquist, *Metrologia* **2018**, *55*, R27.
- [31] R. Ribeiro-Palau, F. Lafont, J. Brun-Picard, D. Kazazis, A. Michon, F. Cheynis, O. Couturaud, C. Consejo, B. Jouault, W. Poirier, F. Schopfer, *Nat. Nanotechnol.* **2015**, *10*, 965.
- [32] M. Kruskopf, D. M. Pakdehi, K. Pierz, S. Wundrack, R. Stosch, T. Dziomba, M. Götz, J. Baringhaus, J. Aprojanz, C. Tegenkamp, J.

- Lidzba, T. Seyller, F. Hohls, F. J. Ahlers, H. W. Schumacher, *2D Mater.* **2016**, *3*, 041002.
- [33] C. Chuang, Y. Yang, S. Pookpanratana, C. A. Hacker, C.-T. Liang, R. E. Elmquist, *Nanoscale* **2017**, *9*, 11537.
- [34] K. Kumar, Y. S. Kim, E. H. Yang, *Carbon* **2013**, *65*, 35.
- [35] M. Souto, K. Strutyński, M. Melle-Franco, J. Rocha, *Chem. Eur. J.* **2020**, *26*, 10912.
- [36] S. Tanabe, Y. Sekine, H. Kageshima, M. Nagase, H. Hibino, *Phys. Rev. B* **2011**, *84*, 115458.
- [37] J. A. Alexander-Webber, J. Huang, D. K. Maude, T. J. B. M. Janssen, A. Tzalenchuk, V. Antonov, T. Yager, S. Lara-Avila, S. Kubatkin, R. Yakimova, R. J. Nicholas, *Sci. Rep.* **2016**, *6*, 30296.
- [38] X. Tian, J. Xu, X. Wang, *J. Phys. Chem. B* **2010**, *114*, 11377.
- [39] H. Pinto, R. Jones, J. P. Goss, P. R. Briddon, *J. Phys.: Condens. Matter* **2009**, *21*, 402001.
- [40] W. Chen, D. Qi, X. Gao, A. T. S. Wee, *Prog. Surf. Sci.* **2009**, *84*, 279.
- [41] T. H. Le, A. Nafady, X. Qu, A. M. Bond, L. L. Martin, *Anal. Chem.* **2012**, *84*, 2343.
- [42] S. Kopylov, A. Tzalenchuk, S. Kubatkin, V. I. Fal'ko, *Appl. Phys. Lett.* **2010**, *97*, 112109.
- [43] J. Ristein, S. Mammadov, T. Seyller, *Phys. Rev. Lett.* **2012**, *108*, 246104.
- [44] E. H. Hwang, S. Adam, S. Das Sarma, *Phys. Rev. B* **2007**, *76*, 195421.
- [45] F. Lafont, R. Ribeiro-Palau, D. Kazazis, A. Michon, O. Couturaud, C. Consejo, T. Chassagne, M. Zielinski, M. Portail, B. Jouault, F. Schopfer, W. Poirier, *Nat. Commun.* **2015**, *6*, 6806.
- [46] T. Janssen, A. Tzalenchuk, R. Yakimova, S. Kubatkin, S. Lara-Avila, S. Kopylov, V. Fal'ko, *Phys. Rev. B* **2011**, *83*, 233402.
- [47] M. Yang, O. Couturaud, W. Desrat, C. Consejo, D. Kazazis, R. Yakimova, M. Syväjärvi, M. Goiran, J. Béard, P. Frings, M. Pierre, A. Cresti, W. Escoffier, B. Jouault, *Phys. Rev. Lett.* **2016**, *117*, 237702.
- [48] J. M. Poumirol, W. Escoffier, A. Kumar, M. Goiran, B. Raquet, J. M. Broto, *New J. Phys.* **2010**, *12*, 083006.
- [49] J. A. Alexander-Webber, A. M. R. Baker, T. J. B. M. Janssen, A. Tzalenchuk, S. Lara-Avila, S. Kubatkin, R. Yakimova, B. A. Piot, D. K. Maude, R. J. Nicholas, *Phys. Rev. Lett.* **2013**, *111*, 096601.
- [50] A. Chatterjee, M. Kruskopf, M. Götz, Y. Yin, E. Pesel, K. Pierz, B. Schumacher, H. Scherer, in *Conference Digest of the 2022 Conference on Precision Electromagnetic Measurements*, IEEE Xplore, **2022**.
- [51] A. F. Rigosi, A. R. Panna, S. U. Payagala, M. Kruskopf, M. E. Kraft, G. R. Jones, B. Y. Wu, H. Y. Lee, Y. Yang, J. Hu, D. G. Jarrett, D. B. Newell, R. E. Elmquist, *IEEE Trans. Instrum. Meas.* **2019**, *68*, 1870.
- [52] M. Kruskopf, A. F. Rigosi, A. R. Panna, D. K. Patel, H. Jin, M. Marzano, M. Berilla, D. B. Newell, R. E. Elmquist, *IEEE Trans. Electron Devices* **2019**, *66*, 3973.
- [53] K. Pierz, M. Götz, E. Pesel, F. J. Ahlers, H. W. Schumacher, *IEEE Trans. Instrum. Meas.* **2011**, *60*, 2455.